Plasma Physics and Controlled Fusion

OPEN ACCESS

RECEIVED
12 February 2026

REVISED
29 March 2026

ACCEPTED FOR PUBLICATION
10 April 2026

PUBLISHED
21 April 2026

PAPER

Ultralow-emittance electron beams from laser wakefield accelerator based on sharp density transition injection

Yanjie Ge[1,2], Ke Feng[1,*], Runshu Hu[1,2], Kangnan Jiang[1], Hai Jiang[1], Xizhuan Chen[1,2], Shixia Luan[3], Wentao Wang[1,*] and Ruxin Li[1,4,*]

[1] State Key Laboratory of Ultra-intense Laser Science and Technology, Shanghai Institute of Optics and Fine Mechanics (SIOM), Chinese Academy of Sciences, Shanghai 201800, People's Republic of China
[2] Center of Materials Science and Optoelectronics Engineering, University of Chinese Academy of Sciences, Beijing 100049, People's Republic of China
[3] School of Electronic and Information Engineering, Ningbo University of Technology, Ningbo 315211, People's Republic of China
[4] School of Physical Science and Technology, ShanghaiTech University, Shanghai 201210, People's Republic of China
[*] Authors to whom any correspondence should be addressed.

E-mail: fengke@siom.ac.cn, wwt1980@siom.ac.cn and ruxinli@siom.ac.cn

Keywords: laser wakefield acceleration, emittance, electron injection

Abstract

We numerically investigate a scheme for generating ultralow-emittance electron beams using hydrodynamic optical-field-ionization (HOFI)-induced shock injection in laser wakefield acceleration (LWFA). A steep density down-ramp formed by the HOFI process enables electron injection at low laser amplitude a_0, reducing transverse forces and favoring longitudinal injection to minimize the beam emittance. Particle-in-cell simulations demonstrate the production of high-quality electron beams with a charge of 28 pC, an energy of approximately 350 MeV, an rms energy spread of about 3%, and a normalized projected emittance of about 80 nm rad. Unlike mechanically driven shocks commonly used in LWFA, the HOFI-induced shock exhibits superior stability, enabling precise control over the electron injection process. Moreover, because injection occurs where a_0 is relatively low and slowly varying, the scheme shows enhanced tolerance to laser energy jitter. This approach provides a promising pathway for generating high-quality electron beams suited for downstream applications such as GeV-class plasma accelerators and free-electron lasers.

1. Introduction

Benefiting from their capability to sustain unprecedented accelerating gradients reaching several hundred gigavolts per meter, laser wakefield accelerators (LWFAs) have attracted significant interest since they were first proposed by Tajima and Dawson [1]. Inspired by the considerable potential of such compact accelerators, tremendous progress has been achieved over the past two decades, including the generation of electron beams carrying nano-Coulomb-level charge [2, 3], energy spread at the sub-percent level [4, 5], emittance on the order of several hundred nm rad [6, 7], and operational stability maintained over durations exceeding 24 h [8]. With the improved beam quality and stability, the lasing of a free-electron laser (FEL) adopting a LWFA has been successfully demonstrated [9, 10].

To advance the practical application of LWFAs, the generation of electron beams with low emittance is essential for preserving beam quality over extended propagation. In FELs, a sufficiently low-emittance electron beam enhances the gain by mitigating longitudinal phase slippage caused by betatron oscillations [11]. In high-energy physics, emittance critically limits the focusability of particle beams, thereby influencing the achievable luminosity and, consequently, the event rate. For future TeV-scale colliders relying on multistage LWFAs [12], reduced emittance is essential for achieving efficient inter-stage coupling [13, 14]. Extensive studies have explored the dynamics in plasma-based accelerators, and the emittance is primarily constrained by the electron injection process. Thus, the injection mechanism has

been widely recognized as the key factor in determining the initial phase space of the beam and, consequently, the attainable emittance [15–17]. In addition, to preserve beam quality and its ultimate performance in subsequent stages, various strategies for preserving emittance from the source to the end application have also been proposed and actively investigated [18–21]. Notably, studies have demonstrated that emittance can be maintained under high-gradient, high-efficiency plasma wakefield acceleration while simultaneously maintaining beam charge and energy spread [22]. Despite these advances, the achievable emittance often remains insufficient for demanding downstream applications, such as x-ray FELs and colliders, which typically require electron beams with a normalized emittance on the order of 100 nm rad [23–25].

In this work, we investigate the high-quality electron beam generation with ultralow transverse emittance (<100 nm rad) via the hydrodynamic optical-field-ionization (HOFI)-induced shock injection mechanism. The concept of HOFI was first introduced for generating plasma channels capable of guiding intense laser pulses over extended distances [26–28] and has then been adapted for shock-front formation [29–32]. The HOFI-induced shock front, featuring a steep density down-ramp, can trigger electron injection at a relatively low normalized laser amplitude a_0, where the laser-driven transverse force is weaker, thereby reducing emittance growth during injection. Particle-in-cell (PIC) simulations show that the proposed scheme can generate high-quality electron beams with a charge of 28 pC, an energy of approximately 350 MeV, an rms energy spread of about 3%, and a normalized projected emittance of approximately 80 nm rad. In addition, the injection can be controlled to occur at a slowly varying laser amplitude, further suppressing sensitivity to laser jitters from shot-to-shot. The proposed scheme holds great potential for generating high-quality electron beams with superior stability, making it well-suited for applications such as staged acceleration and FELs.

2. Physical mechanism for emittance optimization using HOFI-induced shock injection

Normalized emittance serves as a key parameter for evaluating electron beam quality, quantifying the area occupied by the beam in phase space, and can be defined by $\varepsilon_{n,x} = \sqrt{\langle x^2\rangle\langle p_x^2\rangle - \langle x p_x\rangle^2}/m_e c$, where m_e is the electron rest mass, c is the speed of light in vacuum, and x and p_x are the transverse position and momentum of the particles, respectively. For particle bunches of finite length, the projected emittance represents the overall phase-space extent of the beam.

To investigate the generation mechanism of ultralow emittance electron beams, quasi-three-dimensional PIC simulations are performed using the Fourier–Bessel PIC code [33, 34]. The co-moving simulation box has sizes of 40 μm and 120 μm in the longitudinal and transverse directions, respectively, with a grid resolution of $\Delta z = \Delta r = 20$ nm, and 16 macro-particles per cell. A Gaussian laser pulse has a central wavelength of $\lambda = 800$ nm, a waist radius of $\omega = 27\,\mu$m, and a pulse duration of 28 fs (FWHM), yielding a normalized vector potential of $a_0 = 1.1$. The plasma density profile was selected according to experimentally measured results reported by Miao *et al* [35] and Mewes *et al* [36]. The longitudinal density distribution exhibits a double-peak structure with a low-density region between the peaks within the HOFI interaction region, followed by a density plateau, as shown in figure 1(a). The HOFI-induced shock front extends over a width on the order of 10–20 μm [35, 37], comparable to the local plasma wavelength (approximately 15.6 μm at an electron density of $4.5 \times 10^{18}\,\mathrm{cm}^{-3}$). The specific density profile implemented in the simulation features a plateau density of $n_{\mathrm{plat}} = 4.5 \times 10^{18}\,\mathrm{cm}^{-3}$, a peak density of $n_{\mathrm{peak}} = 9 \times 10^{18}\,\mathrm{cm}^{-3}$, a shock front length of 14 μm, and a distance of approximately 110 μm between the two density peaks, as illustrated in figure 1.

From figure 1(a), it can be observed that injection occurs at a relatively low laser amplitude of $a_0 \approx 2.07$, which is obviously lower than the $a_0 \sim 2.5$ discussed with mechanical shock-induced injection schemes [38]. This lower threshold is achieved while maintaining comparable charge, which is attributed to the steep density down-ramp implemented in the present configuration. Notably, due to the polarization of the drive laser, the electron beam emittance in the laser polarization direction (i.e. the y direction) is typically higher than that in the orthogonal direction (the x direction). After injection, the projected emittance of the electron beam stabilizes at approximately 80 nm rad and exhibits only minor fluctuations during acceleration, as shown in figure 1(a). This indicates that the projected emittance is largely determined by the intrinsic emittance of the electron beam at the injection stage in the presented scheme. Figure 1(b) presents the longitudinal phase space and the energy spectrum of the electron beam at the end of the acceleration. The electron beam energy is approximately 350 MeV, with a relative rms energy spread of about 3%, demonstrating the potential of the presented scheme for generating high-quality electron beams.

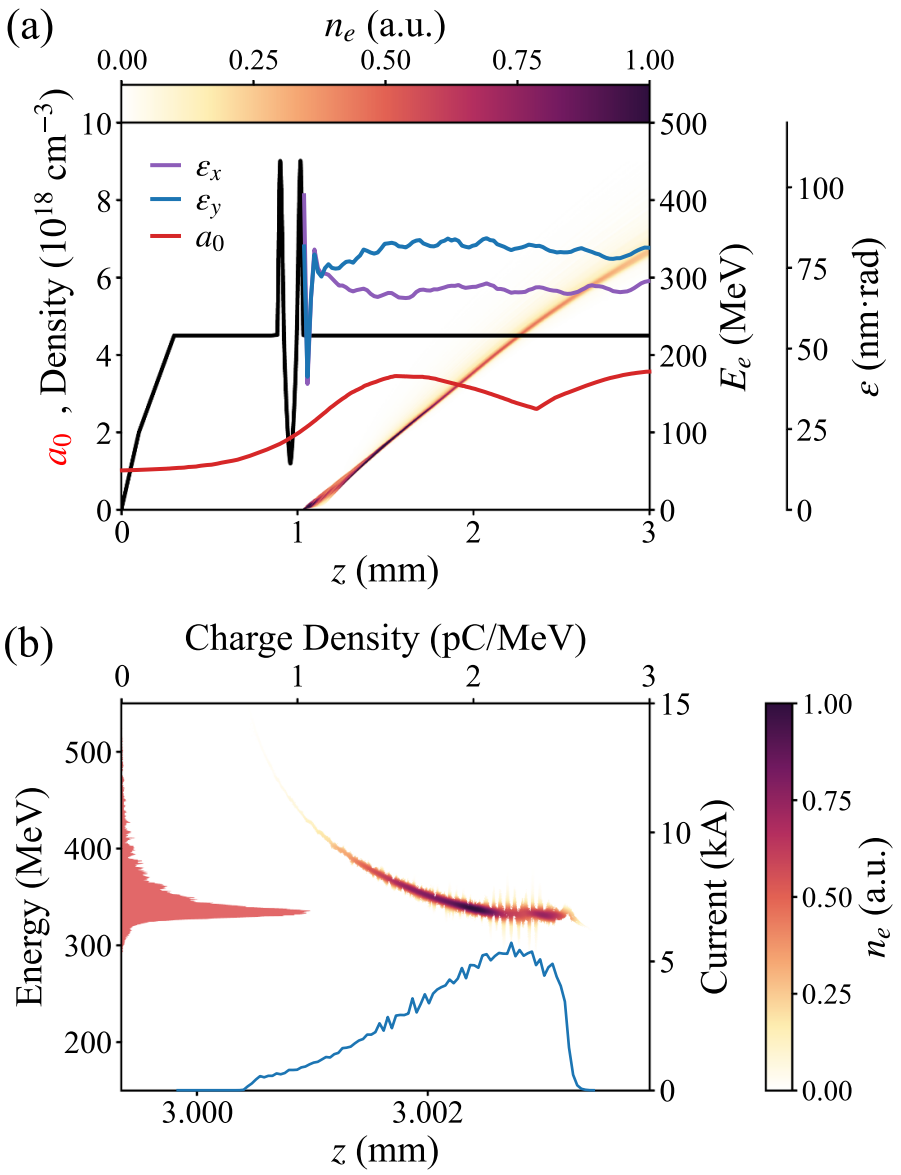

Figure 1. Particle-in-cell simulation of ultralow-emittance beam generation in LWFA. (a) Evolution of the beam and laser-plasma parameters during acceleration. The black, red, purple, and blue curves denote the plasma density profile, normalized laser amplitude a_0, and normalized projected emittances ϵ_x and ϵ_y, respectively. The plasma density profile in the simulation starts with an initial rising edge, followed by a plateau region at a density of n_{plat}. At the longitudinal position of 0.886 mm, an HOFI-induced channel structure is introduced, followed by another plateau region at the same density. (b) Simulation snapshots at the longitudinal position of 3 mm, and the blue curve denotes the beam current.

The projected emittance can be understood as consisting of two components: the slice emittance and the chromatic emittance. The slice emittance characterizes the intrinsic transverse phase-space area occupied by each longitudinal slice of the beam, whereas the chromatic emittance quantifies the phase-space decoherence among different slices, which typically arises from mismatches in betatron phase or beam size. The projected emittance can be optimized down to its slice emittance if each temporal slice is aligned in phase space. In the present simulations, the longitudinal slice length is set by the numerical resolution, with a slice thickness of $\delta z = 20$ nm. As shown in figure 2(a), the black and blue solid lines represent the evolution of the projected emittance and the slice-averaged emittance of the electron beam along the propagation direction during the early stage of acceleration, respectively. It can be seen that, in this stage, the projected emittance first decreases markedly and then increases rapidly during the subsequent acceleration, whereas the slice emittance remains relatively smooth throughout the process and stays at a consistently low level.

To explore the mechanism of the obtained ultralow-emittance electron beam, the dynamics of the electrons during the injection process need to be analyzed, with particular emphasis on their transverse

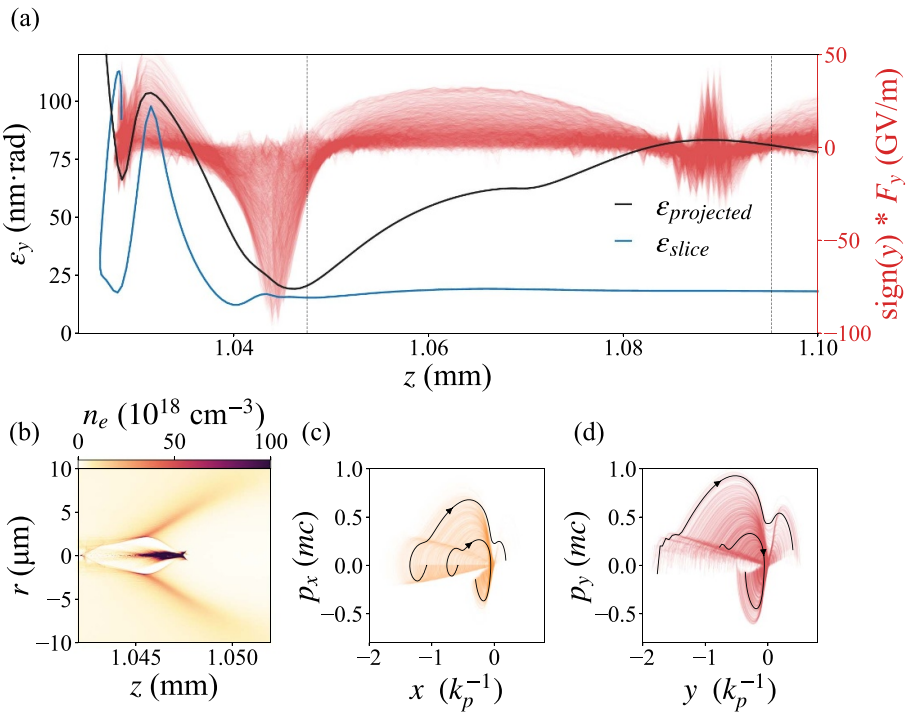

Figure 2. (a) The evolution of emittance in the polarization direction and the defocusing field in the same direction experienced by the central part of the electron beam during the injection process. The dashed lines mark the locations used for the analysis in figure 3. (b) Snapshot of the electron beam at an early stage of injection. (c) and (d) Transverse phase-space trajectories of the injected electrons in the central longitudinal slice of the bunch, selected for electrons with initial transverse positions $x_i < 0$ (or $y_i < 0$).

dynamics. The effective transverse fields experienced by the electrons are shown in figure 2(a), which are described by $\mathrm{sign}(y) \cdot F_y$, where $F_y = E_y + c\beta_z B_x - c\beta_x B_z$. The corresponding Lorentz force in the y direction is given by $e \cdot F_y$, and a negative value of $\mathrm{sign}(y) \cdot F_y$ indicates an outward force from the axis, i.e. a defocusing effect.

Considering the very beginning of the laser plasma interaction, when the laser arrives, an electron with nearly zero initial transverse momentum is displaced off-axis by the ponderomotive force of the laser. As the interaction evolves, the plasma-induced restoring force pulls the electron back toward the axis, thereby increasing its transverse momentum. In addition, along the laser polarization direction, the electron undergoes strong oscillations driven by the transverse electric field, which also contribute to the growth of the beam emittance. Once the electron exits the main intensity region of the laser pulse, it begins to experience a focusing field generated by the wakefield, which further drives it toward the axis and initiates rotation in the transverse phase space. When the electron approaches the axis, the local space-charge density increases. At this stage, the laser intensity is not yet sufficiently high to drive a strong wakefield, the increased charge density leads to significant beam loading effects, giving rise to a defocusing field with a strength on the order of 100 GV m^{-1}, as shown in figure 2(b).

This defocusing field effectively reduces the electron's transverse velocity, leading to a contraction of its phase space trajectory and a consequent decrease in transverse emittance. With continued laser self-focusing and increasing intensity, the plasma bubble forms, the defocusing field evolves into a focusing one, and the electron's transverse phase-space rotation continues. This entire evolution of the transverse phase space, including the defocusing-induced contraction and subsequent rotation, is illustrated in figures 2(c) and (d). It is noteworthy that, due to the polarization of the laser, the electron's transverse trajectory in this direction exhibits significant oscillations during the early stage of the interaction. The corresponding trajectories in the transverse phase space appear highly disordered at this stage, which tends to obscure the subsequent evolution of interest. Therefore, to ensure the clarity of the illustration, we only show the transverse phase space trajectory of the electron beam after it exits the main intensity region of the laser pulse in this direction, as depicted in figure 2(d).

At the initial stage of injection, the projected emittance of the electron beam is low, approximately 20 nm rad, with most electrons concentrated around similar betatron phases. As a result, the beam occupies only a small region in transverse phase space, as shown in figure 3(a). At this stage, the electron beam exhibits a pronounced negative energy chirp. Owing to the relatively low laser intensity during

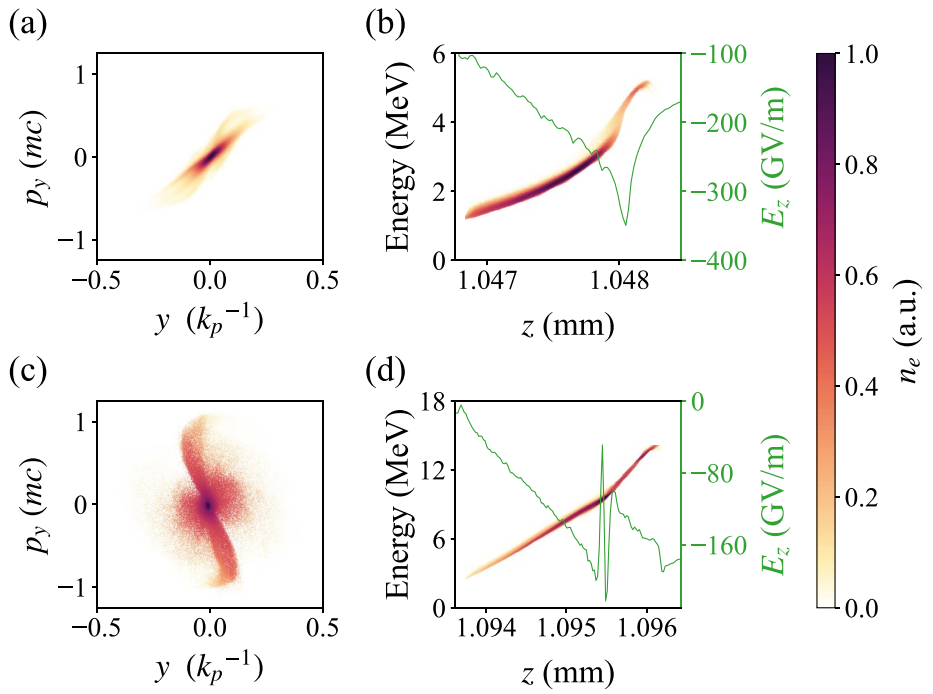

Figure 3. (a) and (c) Transverse y–p_y phase space of the electron beam at the two locations indicated by the vertical dashed lines in figure 2(a). (b) and (d) Corresponding longitudinal phase space and on-axis acceleration field (green lines).

injection, beam loading effects are significant, leading to a stronger accelerating field experienced by the head of the beam and a weaker one at the tail. This non-uniform accelerating field further enhances the negative energy chirp. Moreover, since the beam energy is still relatively low at this stage, the pronounced energy chirp readily translates into longitudinal velocity differences, resulting in a noticeable elongation of the beam length.

During acceleration, electrons undergo transverse oscillations at the betatron frequency $\omega_\beta = \omega_\mathrm{p}/\sqrt{2\gamma}$, where ω_p is the plasma frequency and γ is the relativistic factor. This energy dependence causes different longitudinal slices to rotate at different rates in transverse phase space, thereby enhancing phase-space decoherence and ultimately leading to an increase in the projected emittance through transverse phase-space spreading. Within a propagation distance of approximately 50 μm, the projected emittance rapidly increases to about 80 nm rad, and the phase distribution of the beam extends over nearly the full 0–2π range, as clearly illustrated in figure 3(c). In the subsequent acceleration process, once the phase difference between the head and tail of the beam exceeds π, the longitudinal slices reach a fully decoherent state. In this regime, the projected emittance exhibits only mild oscillations, which mainly correspond to dephasing and rephasing processes.

Although the electron beam is fully decohered under such conditions, its projected emittance remains relatively low because the small slice emittance sets the lower bound of the total emittance. At the early stage of acceleration, the bunch length rapidly increases from less than 1 μm to nearly 3 μm and remains stable thereafter. As shown in figure 4(a), the slice emittance in the polarization direction exhibits distinct evolution behaviors across different longitudinal positions. In this stage, frame-to-frame fluctuations are observed in the raw slice emittance data, making the overall evolution trend difficult to discern. These variations may originate from limited particle statistics within individual longitudinal slices and the temporal sampling interval. To suppress such fluctuations and better reveal the overall trend, a temporal moving average was applied to the emittance data. The resulting smoothed profile, shown in the inset of figure 4(a), presents a clearer and more interpretable evolution while retaining the key physical features. The emittance at the beam tail exhibits a continuous increase; however, as shown in the current profile of figure 1(b), the current is relatively low in this region. Consequently, its contribution to the overall beam emittance is negligible and thus not discussed further.

In an ideal linear focusing system, the beam emittance can be preserved. However, in the wakefield, the transverse focusing field experienced by the electrons is inherently nonlinear, particularly when beam loading effects are pronounced, rendering slice emittance growth unavoidable. As shown in figure 4(a), the slice emittance along the polarization direction exhibits four distinct stages: an initial sharp decrease, a rapid increase, a secondary decrease, and a slight final rise. This evolution reflects the interplay

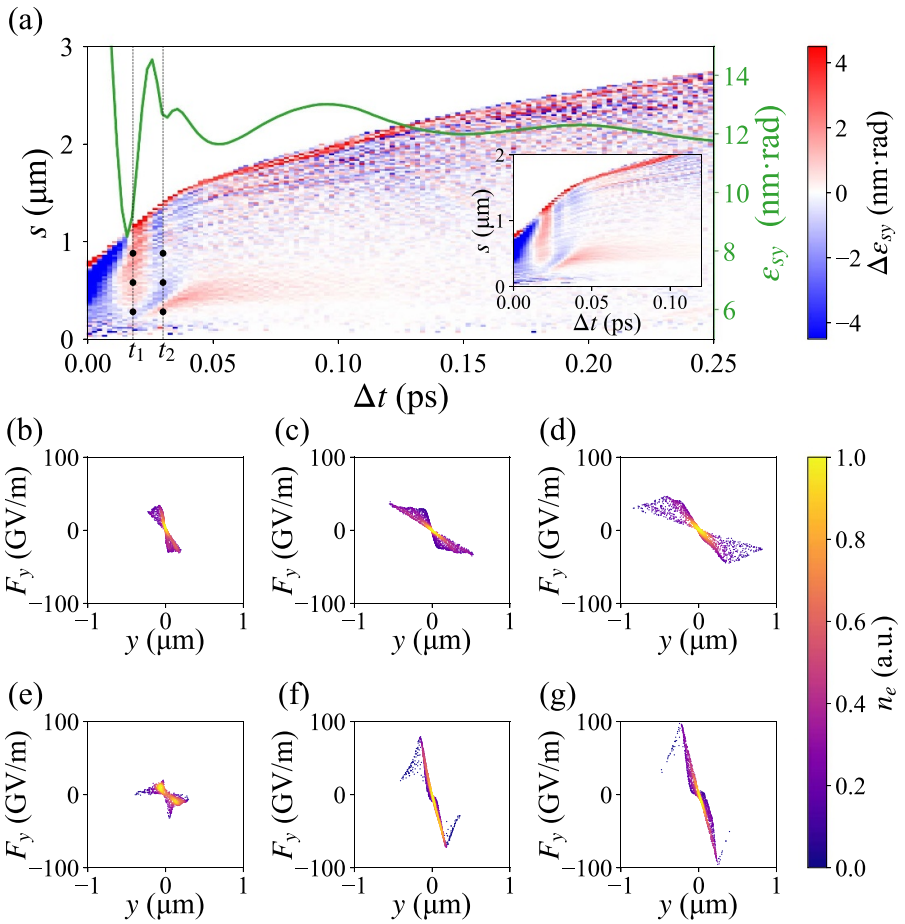

Figure 4. (a) Time evolution of the slice emittance variation $\Delta\varepsilon_{sy}$ along the beam longitudinal coordinate s, where $\Delta\varepsilon_{sy}$ (shown in color scale) represents the change in slice emittance relative to the previous iteration, defined as $\Delta\varepsilon_{sy}(s, \Delta t_n) = \varepsilon_{sy}(s, \Delta t_n) - \varepsilon_{sy}(s, \Delta t_{n-1})$. The green line shows the evolution of the average slice emittance ε_{sy}. The time axis represents relative time. The inset shows the result after applying a temporal moving average to the raw slice emittance data to reduce fluctuations and reveal the overall trend. (b)–(g) Transverse field F_y distributions along the y direction at selected positions marked in panel (a). Panels (b)–(d) correspond to the beam profile at t_1, and panels (e)–(g) correspond to t_2. For each time point, the three subplots represent different longitudinal positions s within the bunch, corresponding to slices in the head, center, and tail of the beam, respectively.

between nonlinear focusing dynamics and beam structure: at time t_1, during the transition from a focusing to a defocusing field (figures 4(b)–(d)), the tail region experiences increasingly nonlinear defocusing fields. The resulting phase space distortion and mixing outweigh the contraction effects, leading to a pronounced emittance growth in the tail, while the head—with weaker nonlinearities—continues to decrease in emittance. At time t_2, the situation reverses: the tail encounters a more linear defocusing field and shows a decrease in emittance, while the head, subject to stronger nonlinearities, exhibits emittance growth, as illustrated in figures 4(e)–(g). Subsequently, more slices in the front–middle region experience a transition of the transverse field into the nonlinear regime, leading to an increase in emittance and thereby driving an overall growth in the slice emittance. For the tail, although residual distortions persist at the edges of the transverse field, their influence on the overall evolution remains limited. Thereafter, as the field gradually returns to a focusing regime, the slice emittance increases slowly with mild oscillations. Overall, the beam loading–induced nonlinearity of the transverse field plays an important role in the evolution of the slice emittance.

3. Discussion

It is worth noting that while our injection threshold of $a_0 \approx 2.07$ is lower than that typically associated with mechanical shock-induced injection ($a_0 \sim 2.5$), other injection mechanisms, such as optical injection, ionization injection, and self-injection under certain conditions, can achieve injection at even lower laser amplitudes. However, a distinct advantage of our HOFI-induced shock scheme is its ability to

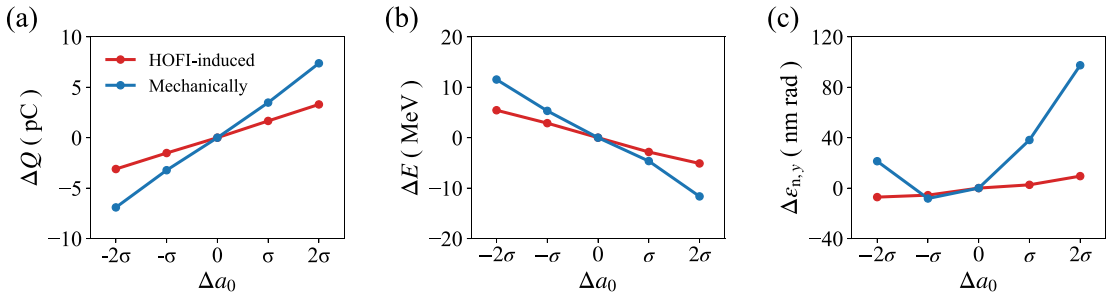

Figure 5. Dependence of the relative deviations in injected beam charge ΔQ (a), energy ΔE (b), and normalized projected emittance in the polarization plane $\Delta\epsilon_{n,y}$ (c) on the laser amplitude deviation Δa_0 for HOFI-induced and mechanically driven shock injection.

stably produce high-quality electron beams with an ultralow normalized projected emittance of approximately 80 nm rad while maintaining a substantial beam charge (∼28 pC), without relying on the complex multiple-pulse alignment typical of optical injection schemes. This emittance level is comparable to or lower than typical values reported for other injection mechanisms, such as ∼1000 nm rad for ionization injection [39], ∼170 nm rad for optical injection [40], ∼10 nm rad for two-color laser schemes [41], ∼60 nm rad for resonant multi-pulse ionization injection [42], and ∼100 nm rad for self-injection with sub-pC charge [43].

Furthermore, compared with conventional shock-generation methods that rely on mechanical techniques, this HOFI-based approach significantly enhances the stability of the injection process. Since injection occurs at a relatively low normalized laser amplitude a_0 and under slowly varying conditions, the scheme exhibits improved tolerance to laser energy fluctuations. Under our current experimental conditions, with an rms laser energy jitter of approximately 0.54%, the injected charge fluctuation in the HOFI-driven scheme remains within ±3.30 pC over a $\pm 2\sigma$ variation range, as shown in figure 5. For comparison, in a mechanically driven scheme simulated under the same $\pm 2\sigma$ laser jitter [38], the injected charge fluctuation reaches ±7.37 pC. Additionally, the normalized projected emittance in the HOFI-driven scheme varies by less than 20 nm rad, whereas that of the mechanically driven scheme shows a significantly larger variation of approximately 100 nm rad. These results further confirm the improved jitter tolerance of the present scheme.

In conclusion, we propose a scheme for generating ultralow-emittance electron beams via shock injection induced by HOFI. In this scheme, the steep density down-ramp created by HOFI allows electron injection to take place at a relatively low normalized laser amplitude a_0, while the injected charge evolves in a gradual and self-consistent manner as a_0 changes. This injection regime provides favorable conditions for achieving a controlled injected charge together with preserved beam quality, and the reduced sensitivity of the injection process to the drive laser parameters further enhances the robustness of the scheme. As a result, an ultralow-emittance electron beam with a charge of 28 pC and a transverse emittance of approximately 80 nm rad is obtained. These features make this method a promising route toward stable generation of high-quality electron beams, well suited for downstream applications such as GeV-class accelerators and FELs.

Data availability statement

The data cannot be made publicly available upon publication because they are not available in a format that is sufficiently accessible or reusable by other researchers. The data that support the findings of this study are available upon reasonable request from the authors.

Appendix A. Sensitivity analysis of the injection scheme

To further evaluate the robustness of the HOFI-induced shock injection scheme against typical experimental fluctuations, we examined the sensitivity of the injected beam quality to variations in the density down-ramp length (L_{ramp}), the laser waist radius (w_0), and the pulse duration (τ).

Figure 6(a) shows the effect of varying the density down-ramp length by up to ±25%. As the ramp length increases, the injected charge decreases from about 38 pC to 20 pC, while the normalized projected

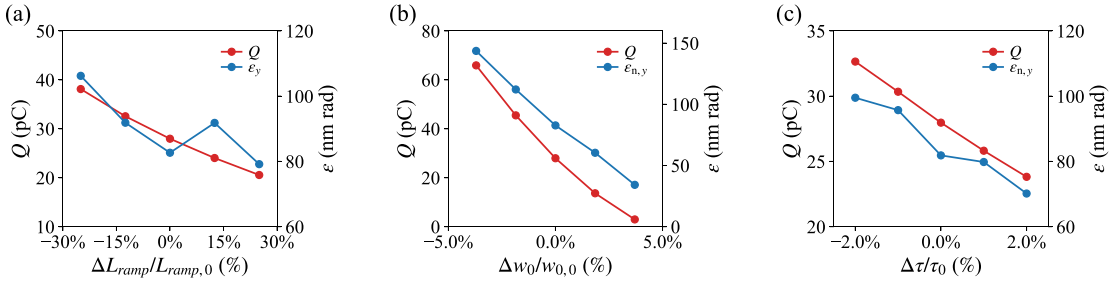

Figure 6. Sensitivity of the injected beam charge (Q, red lines) and normalized projected emittance ($\varepsilon_{n,y}$, blue lines) to variations in (a) the density down-ramp length $\Delta L_{\mathrm{ramp}}/L_{\mathrm{ramp},0}$, (b) the laser waist radius Δw_0, and (c) the laser pulse duration $\Delta\tau/\tau_0$.

emittance remains within $80-100$ nm rad. This indicates that the emittance is relatively insensitive to moderate variations in the ramp length.

Figures 6(b) and (c) show the sensitivity to the initial laser parameters at constant laser energy. As shown in figure 6(b), when the laser waist radius varies by $\pm1\,\mu$m, the injected charge decreases significantly for larger waists, while the emittance is reduced to less than 40 nm rad. A similar but weaker trend is observed in figure 6(c) for pulse-duration variations within $\pm2.0\%$: a longer pulse leads to a slight reduction in both the injected charge (from about 33 pC to 24 pC) and the emittance (from about 100 nm rad to 70 nm rad).

Overall, these results show that although the injected charge changes with the parameters considered here, the scheme retains low emittance over a realistic range of parameter fluctuations.

Appendix B. Numerical convergence of the simulations

To assess the numerical reliability of the ultralow-emittance results, we performed convergence tests with respect to the grid resolution ($\Delta z=\Delta r=\Delta$) and the number of macroparticles per cell (N_{ppc}). As shown in figure 7, the baseline configuration ($\Delta=20$ nm, $N_{\mathrm{ppc}}=16$) is compared with a higher-resolution case ($\Delta=10$ nm, $N_{\mathrm{ppc}}=16$) and a higher-macroparticle case ($\Delta=20$ nm, $N_{\mathrm{ppc}}=32$). Owing

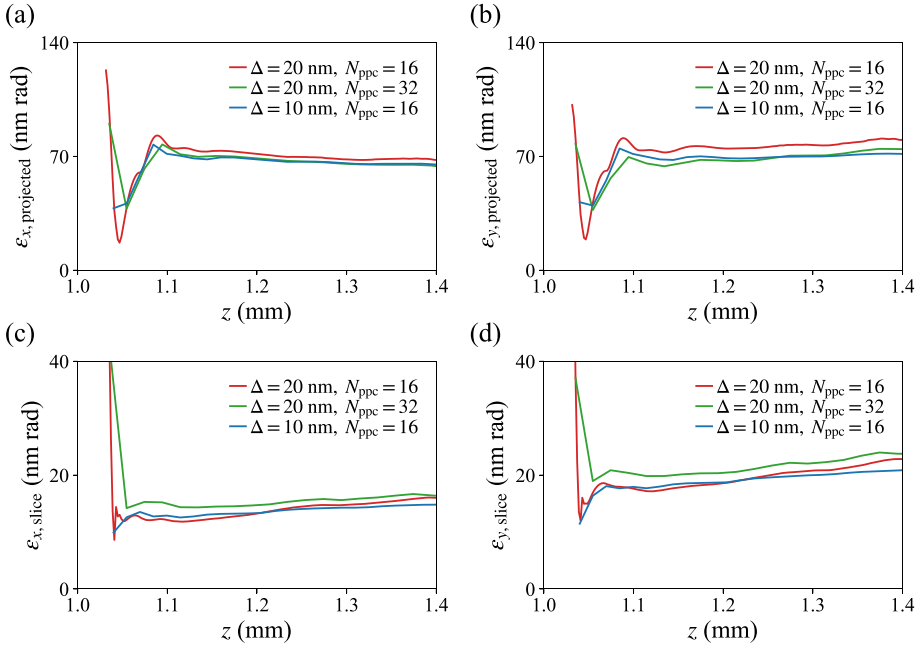

Figure 7. Numerical convergence test results. Evolution of the normalized projected emittances in the laser polarization direction y (a) and the orthogonal direction x (b), alongside the slice-averaged emittances in the y (c) and x (d) directions, along the propagation distance z. The red, green, and blue solid lines represent the baseline case ($\Delta=20$ nm, $N_{\mathrm{ppc}}=16$), the high-macroparticle number case ($\Delta=20$ nm, $N_{\mathrm{ppc}}=32$), and the high-grid resolution case ($\Delta=20$ nm, $N_{\mathrm{ppc}}=16$), respectively.

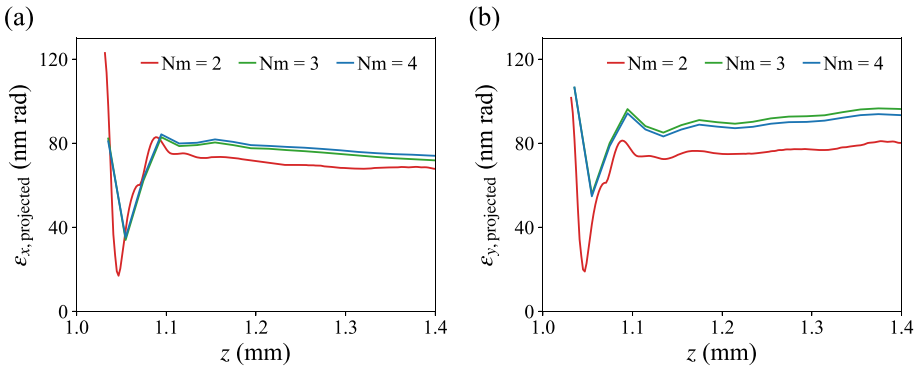

Figure 8. Azimuthal mode convergence test. Evolution of the normalized projected emittance along the propagation distance z in the x (a) and z (b) directions. The red, green, and blue solid lines represent the simulation results using 2, 3, and 4 azimuthal modes (N_m), respectively.

to the substantially increased computational cost, these additional tests were carried out up to a propagation distance of $z = 1.4$ mm, by which the electron injection process is essentially complete and the emittance evolution has approached a stable plateau. The evolutions of both the projected and slice-averaged emittances show good agreement among the three cases. This indicates that the numerical parameters adopted in the main simulations ($\Delta = 20$ nm, $N_{\text{ppc}} = 16$) are sufficient to support the main conclusion.

Furthermore, we assessed the limitation associated with the quasi-3D geometry. In quasi-3D PIC simulations, the electromagnetic fields and currents are expanded into a finite number of azimuthal Fourier modes (N_m), which may limit the capture of higher-order asymmetric transverse dynamics. Figure 8 shows the evolution of the normalized projected emittance for $N_m = 2$, 3, and 4. The results indicate that the emittance evolution in the x direction is largely insensitive to the number of modes. In the y direction, increasing N_m from 2 to 3 leads to a moderate increase in the projected emittance (from ~80 nm rad to ~100 nm rad), indicating the inclusion of additional asymmetric effects. The negligible difference between the $N_m = 3$ and $N_m = 4$ cases suggests that the simulations are close to convergence with respect to the azimuthal mode number. Although full 3D simulations may yield slightly higher emittance values in the y plane than the baseline $N_m = 2$ case, the converged value remains within the ultralow-emittance regime, and the main conclusion of this work is unchanged.

ORCID iDs

Yanjie Ge 0009-0004-5650-6585
Ke Feng 0000-0003-0157-1297
Runshu Hu 0009-0008-1478-8499
Kangnan Jiang 0000-0002-7151-424X
Hai Jiang 0009-0002-9759-8805
Xizhuan Chen 0009-0003-6170-4415
Shixia Luan 0000-0002-6737-1418
Wentao Wang 0000-0002-6339-4858
Ruxin Li 0000-0001-8241-3324

References

[1] Tajima T and Dawson J M 1979 *Phys. Rev. Lett.* **43** 267
[2] Couperus J P *et al* 2017 *Nat. Commun.* **8** 487
[3] Götzfried J *et al* 2020 *Phys. Rev. X* **10** 041015
[4] Wang W T *et al* 2016 *Phys. Rev. Lett.* **117** 124801
[5] Ke L T *et al* 2021 *Phys. Rev. Lett.* **126** 214801
[6] Barber S K *et al* 2017 *Phys. Rev. Lett.* **119** 104801
[7] Jiang K, Feng K, Wang H, Yang X, Bai P, Xu Y, Leng Y, Wang W and Li R 2023 *High Power Laser Sci. Eng.* **11** e36
[8] Maier A R *et al* 2020 *Phys. Rev. X* **10** 031039
[9] Wang W *et al* 2021 *Nature* **595** 516
[10] Labat M *et al* 2023 *Nat. Photon.* **17** 150
[11] Huang Z and Kim K J 2007 *Phys. Rev. ST Accel. Beams* **10** 034801
[12] Albert F *et al* 2021 *New J. Phys.* **23** 031101

[13] Steinke S et al 2016 Nature 530 190
[14] Adli E et al 2018 Nature 561 363
[15] Xu X L et al 2014 Phys. Rev. Lett. 112 035003
[16] Corde S et al 2013 Nat. Commun. 4 1501
[17] Xu X, Dalichaouch T N, Liu J, Ma Q, Pierce J, Miller K, Yan X and Mori W B 2023 Phys. Rev. Accel. Beams 26 111302
[18] Li X, Chancé A and Nghiem P A P 2019 Phys. Rev. Accel. Beams 22 021304
[19] Zhao Y, An W, Xu X, Li F, Hildebrand L, Hogan M J, Yakimenko V, Joshi C and Mori W B 2020 Phys. Rev. Accel. Beams 23 011302
[20] Ariniello R, Doss C E, Lee V, Hansel C, Cary J R and Litos M D 2022 Phys. Rev. Res. 4 043120
[21] Lindstrøm C A and Thévenet M 2022 J. Instrum. 17 P05016
[22] Lindstrøm C A et al 2024 Nat. Commun. 15 6097
[23] Pellegrini C, Marinelli A and Reiche S 2016 Rev. Mod. Phys. 88 015006
[24] Leemans W and Esarey E 2009 Phys. Today 62 44–49
[25] Schroeder C B, Esarey E, Geddes C G R, Benedetti C and Leemans W P 2010 Phys. Rev. ST Accel. Beams 13 101301
[26] Durfee C G and Milchberg H M 1993 Phys. Rev. Lett. 71 2409
[27] Durfee C G, Lynch J and Milchberg H M 1995 Phys. Rev. E 51 2368
[28] Clark T R and Milchberg H M 1997 Phys. Rev. Lett. 78 2373
[29] Faure J, Rechatin C, Lundh O, Ammoura L and Malka V 2010 Phys. Plasmas 17 083107
[30] Fourmaux S, Ta Phuoc K, Lassonde P, Corde S, Lebrun G, Malka V, Rousse A and Kieffer J C 2012 Appl. Phys. Lett. 101 111106
[31] Scott R H H, Thornton C, Bourgeois N, Cowley J, Rittershofer W, Kleinwächter T, Osterhoff J, Symes D R, Hooker C and Hooker S M 2020 Phys. Rev. Accel. Beams 23 111301
[32] v Grafenstein K et al 2023 Sci. Rep. 13 11680
[33] Lehe R, Kirchen M, Andriyash I A, Godfrey B B and Vay J L 2016 Comput. Phys. Commun. 203 66
[34] Jalas S, Dornmair I, Lehe R, Vincenti H, Vay J L, Kirchen M and Maier A R 2017 Phys. Plasmas 24 033115
[35] Miao B, Rockafellow E, Shrock J E, Hancock S W, Gordon D and Milchberg H M 2024 Phys. Rev. Accel. Beams 27 081302
[36] Mewes S M et al 2023 Phys. Rev. Res. 5 033112
[37] Feder L, Miao B, Shrock J E, Goffin A and Milchberg H M 2020 Phys. Rev. Res. 2 043173
[38] Jiang H, Feng K, Hu R, Zhan Q, Wang W and Li R 2025 arXiv:2503.03718
[39] Maity S, Mondal A, Vishnyakov E and Molodozhentsev A 2024 Plasma Phys. Control. Fusion 66 035015
[40] Lehe R, Lifschitz A F, Davoine X, Thaury C and Malka V 2013 Phys. Rev. Lett. 111 085005
[41] Yu L L, Esarey E, Schroeder C B, Vay J L, Benedetti C, Geddes C G R, Chen M and Leemans W P 2014 Phys. Rev. Lett. 112 125001
[42] Tomassini P et al 2025 Sci. Rep. 15 40794
[43] Plateau G R et al 2012 Phys. Rev. Lett. 109 064802